Harmonizing the photocatalytic activity of g-C3N4 nanosheets by ZrO2 stuffing: From fabrication to experimental study for the wastewater treatment

L. Khezami, M.A. Ben Aissa, A. Modwi, M. Ismail, A. Guesmi, F.K. Algethami, M. Ben Ticha, A.A. Assadi, P. Nguyen-Tri

L. Khezami, M.A. Ben Aissa, A. Modwi, M. Ismail, A. Guesmi, et al.. Harmonizing the photocatalytic activity of g-C3N4 nanosheets by ZrO2 stuffing: From fabrication to experimental study for the wastewater treatment. Biochemical Engineering Journal, 2022, 182, pp.108411. 10.1016/j.bej.2022.108411 . hal-03690985

Harmonizing the photocatalytic activity of g-C_3N_4 nanosheets by ZrO_2 stuffing: from fabrication to experimental study for the wastewater treatment

Lotfi Khezami [1*], Mohamed Ali Ben Aissa[2], Abueliz Modwi[2], Mokhtar Ismail[2], Ahlem Guesmi[1], Faisal K. Algethami[1], Manel Ben Ticha[3], Aymen Amine Assadi,[4] Phuong Nguyen-Tri[5*],

[1] Chemistry Department, College of Science, Imam Mohammad Ibn Saud Islamic University (IMSIU), Riyadh, 11623, Saudi Arabia.

[2] Department of Chemistry, College of Science and Arts, Qassim University, Ar Rass, Saudi Arabia.

[3] Department of Early Childhood, University College of Turabah, Taif University, P.O. Box 11099, Taif 21944, Saudi Arabia.

[4] Laboratory of Advanced Materials for Energy and Environment, University Du Quebec Trois-Rivieres (UQTR), 3351, C.P. 500, Trois-Rivieres, Quebec, G9A 5H7, Canada

[5] Univ Rennes, ENSCR / UMR CNRS 6226, 11 Allée de Beaulieu, 35700, Rennes, France.

*Corresponding authors: lhmkhezami@imamu.edu.sa (L. Khezami), Phuong.nguyen-tri@uqtr.ca (P. Nguyen-Tri)

Abstract

ZrO_2@g-C_3N_4 photocomposite has been prepared from ZrO_2 nanoparticles and g-C_3N_4 nanosheet using methanol via the ultrasonic method. The prepared photocomposite was characterized using XRD, TEM, EDX, DRS, FTIR, and XPS techniques and compared with pure ZrO_2 and g-C_3N_4. A comparative study between the photocatalytic performance of the nanocomposite prepared material with ZrO_2 and g-C_3N_4 used to degrade indigo carmine (IC) dye in an aqueous suspension has been developed. The experimental photodegradation data were asserted to conform to the Lagergren kinetics model, and the fabricated nanocomposite registers a higher rate constant and lower half-life time than pure g-C_3N_4. The findings showed that ZrO_2 nanomaterials were adequately predisposed on the g-C_3N_4 surface, resulting in an expanded surface area and lowering band-gap energy. Furthermore, ZrO_2@g-C_3N_4 heterojunctions fabricated was hindered the recombination of superoxide radicals, electrons, and holes and resulted in the magnified photodegradation of IC dye.

Keywords*:* ZrO_2@g-C_3N_4 photocomposite; XPS; IC dye photodegradation: pH efficacy

1- Introduction

Lately, researchers have concentrated on two-dimensional (2D) nanomaterials because of their large specific surface area, the high amount of existing active sites, and unique optical and electrical characteristics [1, 2]. Amongst them, g-C_3N_4 (graphite-carbon nitride) has attracted expanding interest in the photocatalysis domain in an environment due to its 2D graphene-like construction along with its features of non-poisonous, stable, plentiful [3, 4] and lowering band-gap width near ≈2.75 eV [5-7]. Notwithstanding, the g-C_3N_4 received using the conventional thermal decomposition process regularly manifests bulk structure; the low specific surface areas and quick recombination of photo-generated charge carriers considerably restrict its more usage [8-10].

These different important characteristics of g-C_3N_4 encourage its application for visible illuminated photocatalytic purposes employing solar energy. Besides, g-C_3N_4 is abundant and simplistic fabricated through one-stage polymerization of affordable feedstocks similar to urea [11, 12], dicyandiamide [13], thiourea [14], melamine [15], and cyanamide [16, 17]. Although, purely g-C_3N_4 suffers from deficiencies such as accelerated recombination of photo-created electron-hole pairs, a low specific surface area, and a lowering visible light application performance [13, 15, 18, 19]. Then, investigate easy and reliable approaches to manufacturing the g-C_3N_4 nanomaterials based on application as photocatalysts with enhanced physicochemical features and great photocatalytic performance.

Newly, various efforts and strategies have been manipulated to magnify the visible light photocatalytic activity of g-C_3N_4, for instance, the development of heterojunction employing such as TiO_2@g-C_3N_4 [20], ZnO@g-C_3N_4 [21], Bi_2WO_3@g-C_3N_4 [22], CdS@g-C_3N_4 [23], which can comprehensively grow the utilization of the g-C_3N_4 as nanocomposites. Furthermore, limited nanomaterials can couple with g-C_3N_4 to form a heterojunction composition. The critical requirement to develop an adequate visible-light-induced g-C_3N_4 based nanocomposite is that the nanocomposites should have a suitable band construction that is profitable to generate a coupling hybridization structurally.

Depending on the advantages mentioned earlier, the ZrO2@g-C3N4 photocomposite was prepared from its precursors via ultrasonic irradiation. The features of the prepared nanocomposite were investigated, and its possible utilization as a ZrO_2@g-C_3N_4 was examined. A study on the photocatalytic degeneration capability of the IC dye using ZrO_2@g-C_3N_4 nanocomposite at various pH conditions was monitored.

2- Experimental part

2.1. g-C_3N_4 nanosheets fabrication

2.2. ZrO_2@g-C_3N_4 photocatalyst preparation

ZrO_2@g-C_3N_4 photocatalyst was manufactured via a simplistic step ultra-sonication procedure. At first, 920 mg of g-C_3N_4 nanosheet was weighted and sonicated in 0.150 L of methanol solvent for 15min. A 400 mg of ZrO_2 nanomaterials were combined with the methanolic blend, and the resulting mixture was subjected to sonication for 15 min. The yellow collected suspension was subjected to sonication for an extra 45 min and drained in an oven at 363 K for 1440 min. At last, the obtained materials were milled and annealed in a programmed furnace at 453 K for 120 min.

2.3. Characterization

The morphology construction of the specimens was examined through X-ray diffraction (XRD), Bruker AXS, Ger-man, by CuKa radiation source (1.5406 Å) at a scan rate of $0.02.s^{-1}$. A stimulating voltage and selection current of about 40 kV and 20 mA, respectively, were employed. The TEM photographs of pure ZrO_2, g-C_3N_4, and ZrO_2@g-C_3N_4 were performed using a transmission electron microscope, with accelerating voltage 200 kV, via a Tecnai G20 (USA) device. The absorbance in the diffuse reflection method, utilizing barium sulphate as reference, was measured employing a UV-2550 spectrophotometer (Japan). A Nicolet 5700 FT-IR spectrophotometer has served to report the FT-IR spectra of the fabricated specimens on a wavenumber interval ranging from 400 to 4000 cm^{-1}. In order to investigate the chemical bonding and the interaction features of ZrO_2@g-C_3N_4 catalyst with an Al Ka X-ray source (1486.68 eV, VG ESCALAB 220i-XL, UK), XPS (X-ray photoelectron spectroscopy) was operated. The nanocomposites' surface areas and average pore size distributions were studied using the Brunauer-Emmett-Teller (BET) method using a Micromeritics ASAP 2020 apparatus, where samples are outgassed for 120 min, at 150 oC, then weighed and analyzed. The photoluminescence (PL) spectra were measured on the ZrO_2@g-C_3N_4 nanocomposites samples using a fluorescence spectrophotometer (Perkin Elmer LS55) equipped with a xenon lamp, and the selected excitation wavelength is λ =340 nm.

2.4. Photocatalytic degradation experiment details

Indigo carmine (IC) dye has been chosen as a pollutant organic compound to assess the photocatalytic capability for the fabricated ZrO_2@g-C_3N_4 photocomposite. In the conventional photocatalytic trial, 0.050 g of the specimens were suspended separately in 0.100 L IC liquid dye with a fixed concentration of 30 ppm. The degradation of the IC dye was studied in the visible light region at ambient requirements. Before the photocatalytic activity trial, specimen suspension was put in darkness for 30 min and continuously agitated till achieving the equilibrium between the nanomaterials and the IC dye. After adsorption dye equilibrium, 0.05 L of the mixture solution was taken as an original IC concentration (Co). The remaining mixture was then subjected to visible-light radiation (OSRAM lamp 58 IM/W). Then with fixed time intervals, 0.05 L from the suspension was taken and centrifuged for 10 min in order to separate IC dye and estimate its photodegradation. The effectiveness of the photodegradation treatment was evaluated by measuring the difference in the dye concentration via the absorbance measurement at **λ** max = 610 nm using SHIMADZU-UV-1650 PC spectrophotometer.

3. Results and discussions

3.1. XRD confirmation

g-C_3N_4, ZrO_2, and ZrO_2@g-C_3N_4 accumulated XRD models are reported in figure 1. For real g-C_3N_4, characteristic diffraction peaks are located at 2θ =13.0° and 27.58° with interlayer stacking plane (002) of the hexagonal crystal for JCPDS 87-1526 and the in-plane structural sorting motif (100) [24]. The powder x-ray diffraction design of pure ZrO2 nanomaterials is manifested in Fig. 1. The peaks located at two theta angles of 24.00 (110), 28.22 (-111), 31.35 (111), 34.07 (200), 35.27 (002), 40.64 (120), 44.80 (211), 49.24 (220), and 50.09 (022) were matched to monoclinic crystals of ZrO_2 phase for JCPDS No.00-37- 1484 [25, 26]. Besides, the ZrO_2@g-C_3N_4 bands' pattern shows both g-C_3N_4 and ZrO_2 peaks, establishing the precursors rapprochement of in the nanocomposite crystalline composition. The confirmation of the nanocomposite pureness was based on the nonappearance of other crystalline state. Although, the ZrO_2 principal intensity height has changed towards fewer 2θ values from 28.1924 to 28.0514°; meanwhile the FWHM also increased from β = 0.3731° to 0.6128°. These findings may be attributed to the reduction of the crystallite size (D) which was assessed using the Scherrer formula [27]:

$$D = \frac{0.9.\lambda}{\beta.cos\theta}$$

Where:

θ corresponds to the diffraction angle,

β corresponds to the line expanding at half the maximum intensity (FWHM), ʎ corresponds to the wavelength of the Cu Ka radiation,

0.9 corresponds to the dimensionless configuration factor.

Selecting the most intense reflection (-111), the ZrO_2@g-C_3N_4 crystallite was found to be 13.95 nm, while the pure ZrO_2 has D = 23.03nm and absolute g-C_3N_4 equal 7.94 nm.

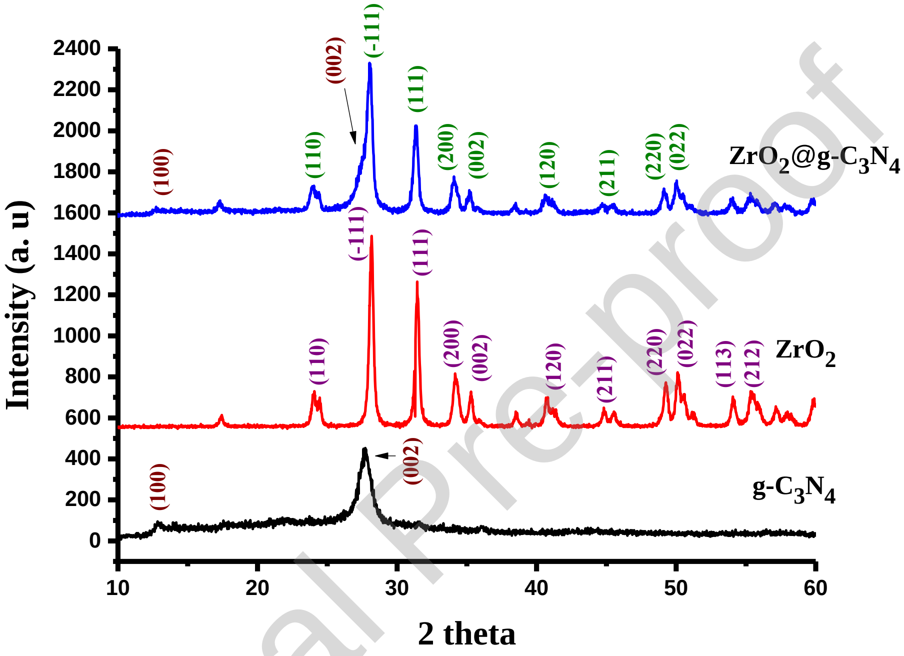

Fig. 1. XRD outlines of g-C_3N_4, ZrO_2, and ZrO_2@g-C_3N_4 photocomposite

3.2. Morphological study

The TEM photographs of the real g-C_3N_4 nanosheets, ZrO_2 nanoparticles, and ZrO_2@g-C_3N_4 hybrid nanostructures are depicted in Figs. 2a, c, and e. The primary g-C_3N_4 TEM picture exhibits soft surface sheets' layers as a common graphitic nanostructure one [28]. On the other hand, the ZrO_2 TEM image (Fig. 2c) presents like-spherical shape nanoparticles with regular size, agreeing with the XRD findings. Furthermore, the TEM photograph (Fig. 2e) of the ZrO_2@g-C_3N_4 photocomposite manifests ZrO_2 nanoparticles separated over the g-C_3N_4 nanomaterials. Therefore, an interface and efficient solid interplay that attaches g-C_3N_4 to ZrO_2

is performed to facilitate the photo-excited charge carriers' detachment for lowering the energy band-gap and improving the photodegradation process. The elemental composition results from the EDS spectrum (Fig. 2b) confirm only C and N for the crumpled layered nanosheet of pure g-C_3N_4. Besides Fig. 2d, the elemental composition of ZrO_2 consists of only Zr and O elements. However, the ZrO_2@g-C_3N_4 reveals the presence of Zr, O, C, and N elements. These results successfully proved the coupling of the ZrO_2 with the g-C_3N_4 nanosheets to develop the photocomposite, as noted in (Fig. 2f).

3.3. Optical properties and DRS calculations

The UV-vis and DRS results of pure g-C_3N_4, ZrO_2, and ZrO_2@g-C_3N_4 photocomposite are presented in Fig. 3. The optical specimen characteristics' findings revealed that the highest absorption wavelength of pure g-C_3N_4 for radiation is 420 nm and for ZrO_2 is about 390.8 nm. Besides, the maximum absorption line edge of ZrO_2@g-C_3N_4 photocomposite is 451.7 nm, and the absorption of visible light is notably improved. Furthermore, these obtained results designate that combining ZrO_2 develops the visible radiation absorption appearance of pure g-C_3N_4. The energy gap estimation was computed employing the Kubelka–Munk equation [29, 30]:

$$\alpha h\nu = A\,(h\nu - E\mathrm{g})^{n/2}$$

Where:

h corresponds to the Plank's constant,

ν corresponds to the light frequency,

α corresponds to the absorption coefficient

Eg is the band-gap and A is a constant,

n is a constituent based on the semiconductor optical transition features (i.e., for direct n = 1 transition, for indirect transition n = 4).

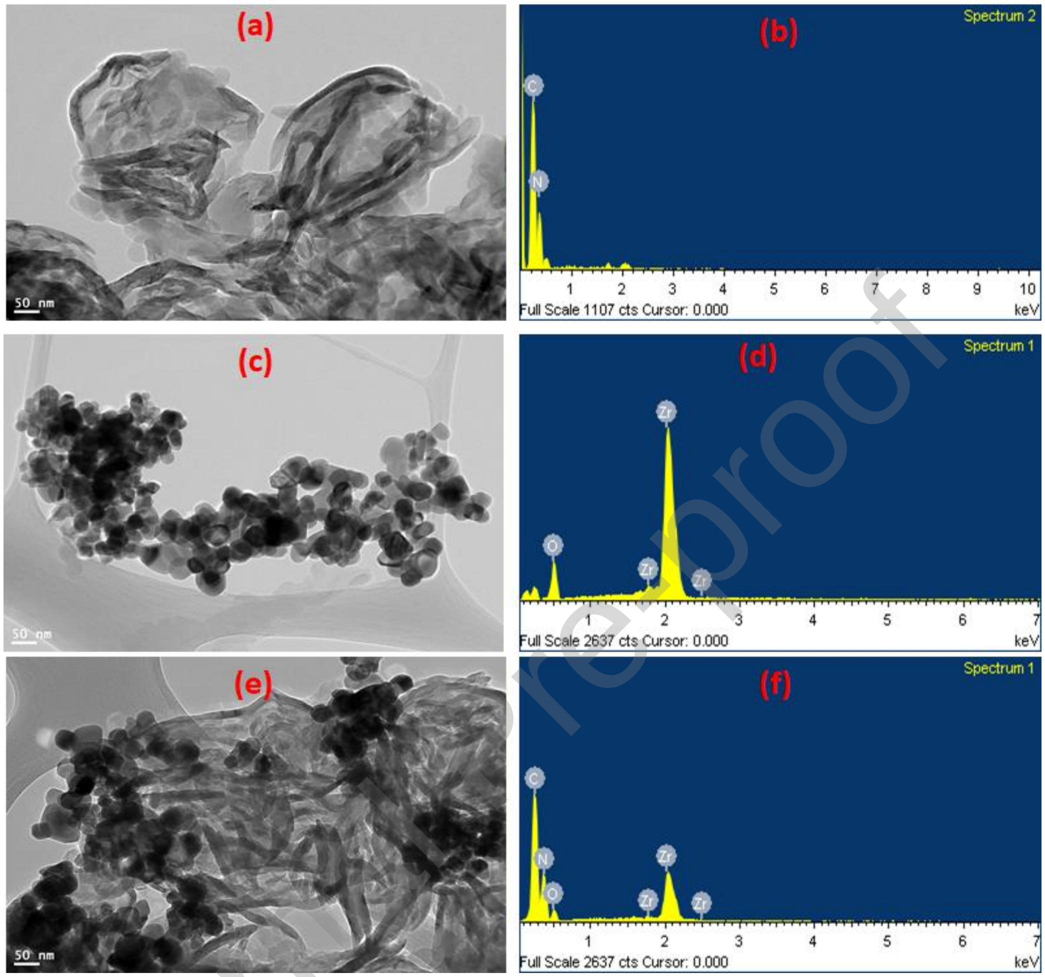

Fig. 2. TEM pictures and EDX (a, b), (c, d), and (e, f) for g-C_3N_4, ZrO_2 and ZrO_2@g-C_3N_4

The energy band gaps of ZrO_2 nanoparticles, g-C_3N_4 nanosheets, and ZrO_2@g-C_3N_4 were counted as 3.64, 2.89 and 2.86 eV, severally. These obtained results were confined to the similar distinguished values in earlier statements [31, 32]. The enhancement of the optical characteristics of photocomposite than purely g-C_3N_4 nanosheets may be owing to the interaction of ZrO_2 nanoparticles with graphitic carbon nitride. In addition to the formation of chemical bonds within the ZrO_2 and g-C_3N_4 also increased visible absorption characteristics.

3.4. FTIR and functional groups determination

The large absorption lines in the FTIR spectrum of purely g-C_3N_4, in the wavenumber range (3500-3000 cm^{-1}) may be attributed to N–H's stretching vibration [33].

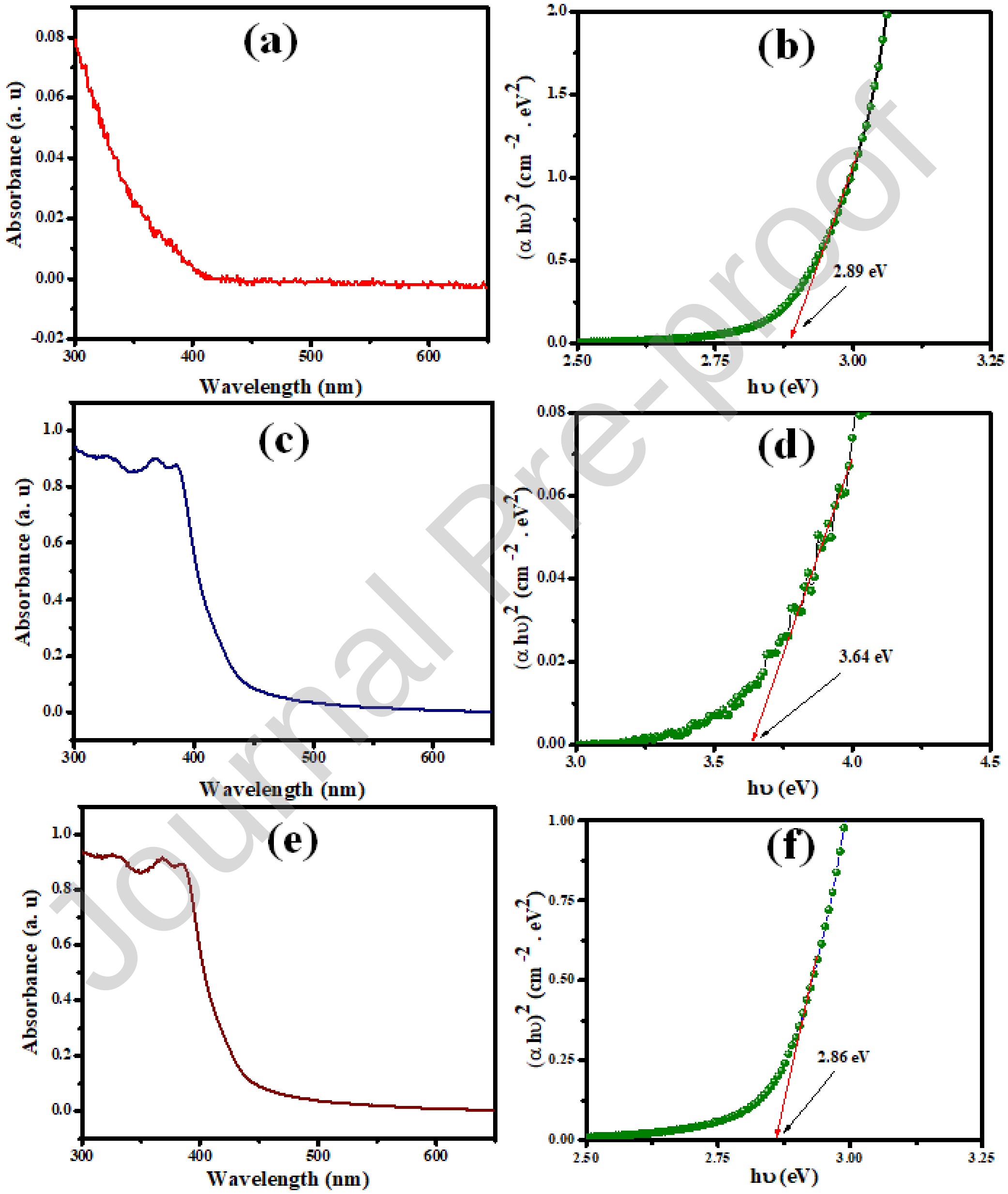

Fig. 3. (a, c, and e) UV-Visible spectra, and (b, d, and f) band-gaps of g-C_3N_4, ZrO_2, and ZrO_2@g-C_3N_4 photocomposite, correspondingly.

In the interval ranging from 1600 to 1200 cm^{-1}, the detected set of bands could be accredited to the common C–N bonds stretching [34]. The presence of a peak located at 810 cm^{-1} is appropriate for the bending vibration of the s-triazine ring, suggesting the existence of hexazine structure in the chemical formation of the as-fabricated g-C_3N_4 nanosheets materials consequently [35].

As shown in (Fig. 4), peaks detected at 1232 cm^{-1} and 1444 cm^{-1}in the FTIR spectra of the ZrO_2 nanopowders are consecutively related to the twisting oscillation of an absorbed water (H_2O) compound and a surface hydroxyl group (OH), [36] A wide vibration band is detected in the wavenumber variety 3330 – 3456 cm^{-1} due to surface hydroxyl group and the absorbed water molecule [37]. The band recognized at 412 cm^{-1} designates the appearance of pure ZrO_2 nanoparticles [38]. The results of pure g-C_3N_4 are similar with FT-IR spectra of ZrO_2@g-C_3N_4, as presented in Fig 4. Notwithstanding, the variation in the peaks at 493.7 to 434.7 cm^{-1} after adding of ZrO_2 clearly confirms the occurrence of the ZrO_2 phase structure. Therefore, these received results reveal the formation of ZrO_2@g-C_3N_4 photocomposite

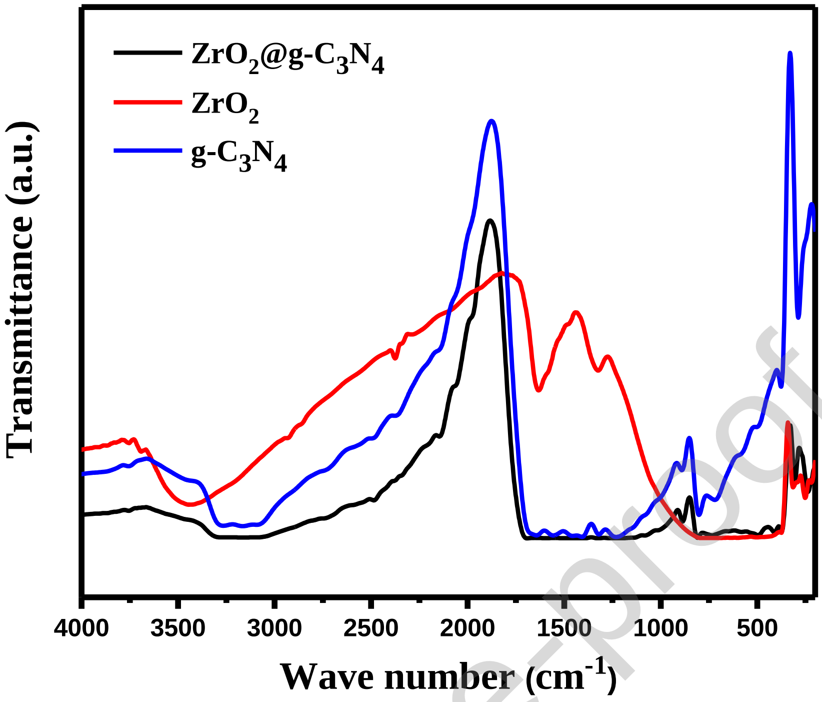

Fig. 4. FTIR *spectra* results for g-C$_3$N$_4$, ZrO$_2$, and ZrO$_2$@g-C$_3$N$_4$ nanomaterials

3.5. XPS analysis

The chemical bonding and configuration of the ZrO$_2$@g-C$_3$N$_4$ surface were observed using the XPS technique, as displayed in Fig. 5(a-d). The XPS chemical outline spectra of the ZrO$_2$@g-C$_3$N$_4$ photocomposite catalyst exhibition just Zr, O, C, and N components revealed the creation amid zirconium oxides (ZrO$_2$) and graphitic carbon nitride (g-C$_3$N$_4$) as in Fig. 5(a-d).

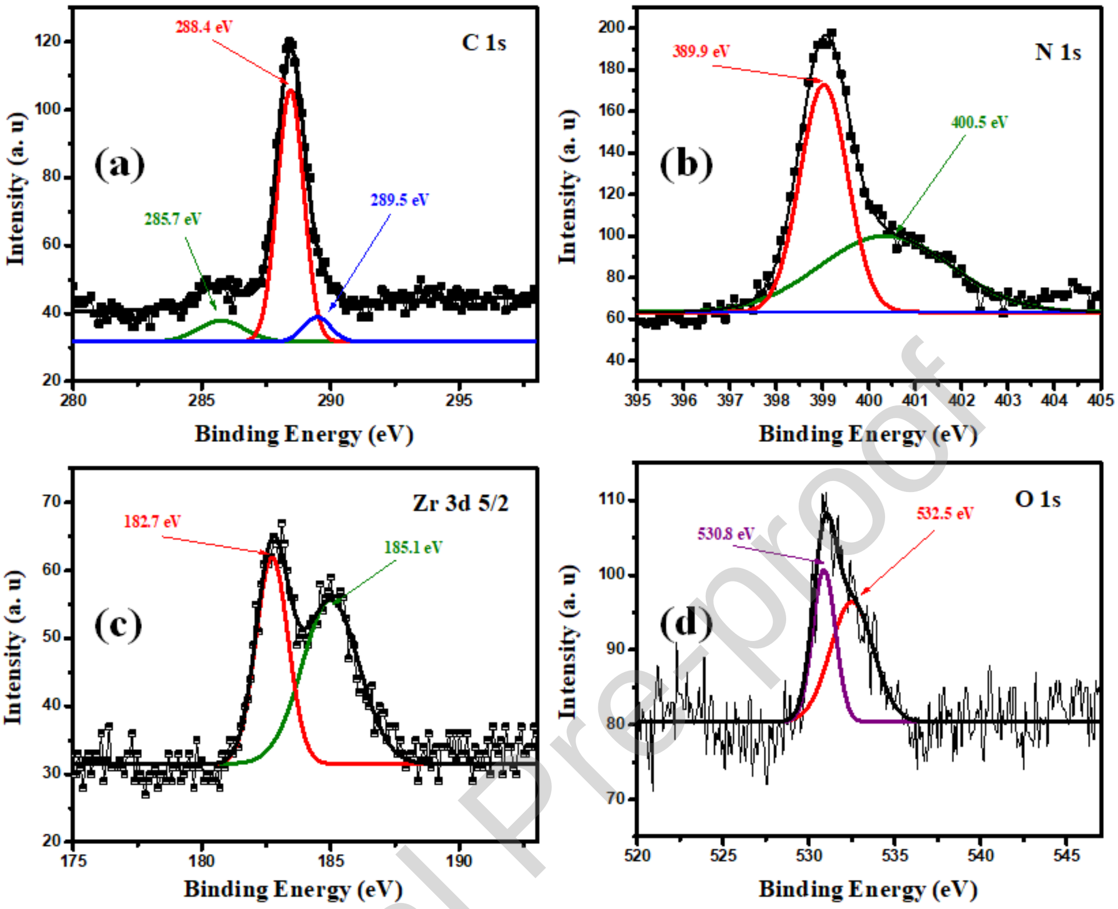

Fig. 5. XPS spectra, (a) C 1s, (b) N 1s, (c) Zr, and (d) O 1s for ZrO_2@g-C_3N_4 photocomposites.

The band is located at 285.7, 288.4, and 289.5 eV for C 1s (Fig. 5(a)), which matches the covalent bond of sp2 hybridized graphic carbon, sp2 carbon chemical bonded to N (N–C=N), and dependency features owing to л – л * excitation, sequentially. [39, 40]. Fig. 5(b) shows the distinct high-resolution peaks for N 1s in ZrO_2@g-C_3N_4 at 389.9 eV, and 404.4 eV can be associated with sp2 hybridized aromatic N incorporated in the triazine structure (C=N–C) and л excitation [41]. The high-resolution peaks at 182.7 and 185.1 eV for Zr 3d could be correlated individually with Zr 3d5/2 and Zr 3d3/2 [42]. The O 1s spectra of ZrO_2@g-C_3N_4 exhibit two bands at 530.8 eV, and 532.5 eV, accredited to the oxygen (O) crystal structure in zirconium oxide and materially adsorbed oxygen, severally as exhibited in Fig. 5(d) [11, 43]. As apparent from the XPS information, the components existing in the ZrO_2@g-C_3N_4 photocomposite are Zr, O, N, and C, managing the incorporation of any impurities. Certain decisions comply with earlier data reported for the ZrO_2@g-C_3N_4 construction [32, 44].

3.6. PL analysis

Photoluminescence spectra were used to examine the effectiveness of photogenerated. Fig. 6 displays the photoluminescence spectra of graphitic carbon nitride (g-C_3N_4) and the ZrO_2@g-C_3N_4 photocomposite at a 360 nm excitation wavelength. As illustrated in Fig. 6, the PL spectra of pure g-C_3N_4 and the ZrO_2@g-C_3N_4 photocomposite exhibit a prominent main emission peak centered at approximately 440 nm, which may be due to electron-hole recombination in g-C_3N_4 [45]. Additionally, the PL intensity of the ZrO_2@g-C_3N_4 photocomposite is lower than that of pure g-C_3N_4, implying that the ZrO_2@g-C_3N_4 photocomposite has a reduced electron-hole recombination rate of electrons and holes when exposed to visible light [46].

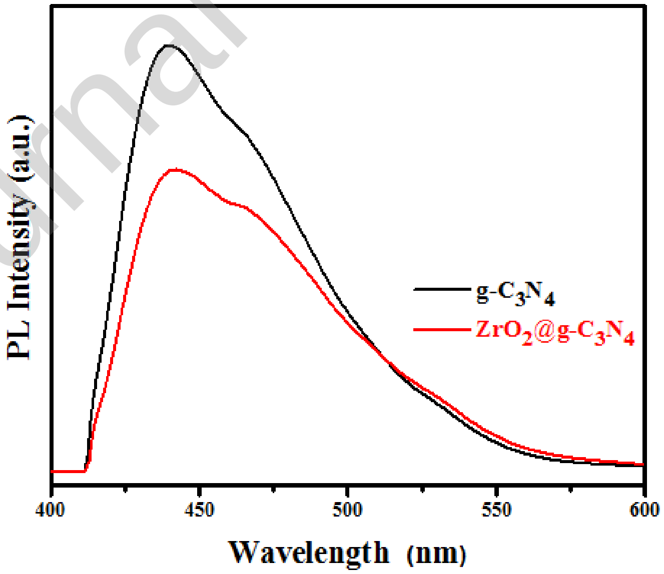

Fig. 6. PL spectra of pure g-C_3N_4, and ZrO_2@g-C_3N_4 photocomposite

3.7. Nanomaterials surface area Assessment

The nitrogen adsorption-desorption isotherms of pure g-C_3N_4 and ZrO_2@g-C_3N_4 nanocomposite are shown in Fig. 7a and b. The isotherms of the ZrO_2@g-C_3N_4 nanostructures are type IV, indicating the presence of mesopores during sample formation due to the weak hysteresis loop generation. Pure g-C_3N_4 specimen display also type IV behavior, explained by the weak hysteresis loop generation [47, 48]. The specific surface area of ZrO_2@g-C_3N_4 nanostructures was 95.685 m^2/g, characterized by a pore volume of 0.216 cm^3/g, which is less than the specific surface area of pure g-C3N4 (154.055 m^2/g and pore volume of 0.912 cm^3/g). Thus, while the large specific surface area of pure and nanocomposite is shown to boost the photocatalytic activity for IC dye degradation, the surface area is not the only factor contributing to the nanocomposite's activity. The charge separation between the two semiconductors is the determining factor in composite production.

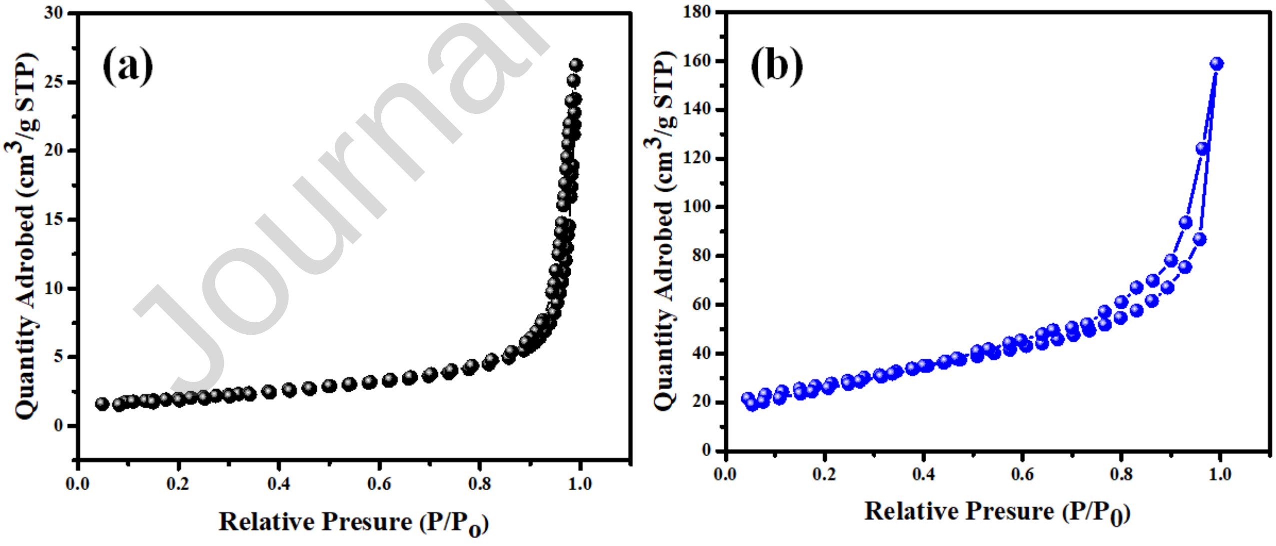

Fig 7: Surface area isotherms characteristics of pure g-C_3N_4 (a), and ZrO_2@g-C_3N_4 photocatalyst (b).

3.7. Photodegradation analysis

3.7.1. The IC dye photodegradation test

The photocatalytic activities of fabricated specimens were observed by decomposing IC dye under visible irradiation. The photodegradation results of IC dye over pure ZrO_2 nanoparticles, pure g-C_3N_4 nanosheets and ZrO_2@g-C_3N_4 photocatalyst under visible light are presented in Fig. 8 (a and b). Before exposition to light, the adsorption equilibrium of IC dye over the nanomaterials was examined in dark conditions, and adsorption balances were reached after 30 min for each specimen. Fig. 8a illustrates the dye photodegradation rates, where C_t and C_o are the concentration of the IC dye at time t and time zero, measured at λ max equal 610 nm.

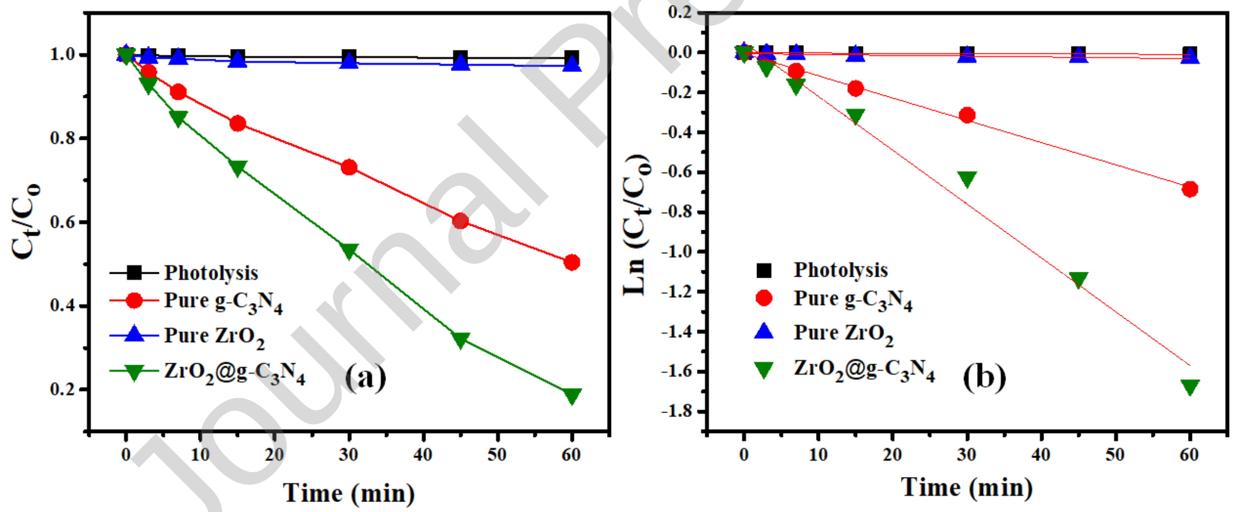

Fig. 8. (a) nanomaterials for IC dye degradation against time, and (b) Lagergren kinetics model.

The photodegradation kinetics of the IC dye obeys the Lagergren kinetics model (Fig. 8b) as designated using the linear correlation of $In(C_0/C_t)$ incremented by the time [49], which is established through the acceptable regression coefficient as shown in Table 1. The developed photocatalytic performance of the ZrO_2@g-C_3N_4 photocomposite is indicated through the high degradation rate constant (*k*) and lower half-life time values recorded in Table 1. The degradation impact of the photocomposite fabricated is five folds of pure g-C_3N_4 nanosheets, proving that the hetero-structured junction within ZrO_2 and g-C_3N_4 is essential for accomplishing enhanced action ZrO_2@g-C_3N_4 photocomposite [32].

Table 1: photocatalysis parameters of IC dye decomposition

Samples	**k (min^{-1})**	**$t_{1/2}$ (min)**	**R^2**	**RSS**
Pure g-C_3N_4	0.00512	135.4	0.99	0.00100
Pure ZrO_2	0.00041	1690	0.89	0.00006
ZrO_2@g-C_3N_4	0.02790	24.84	0.98	0.03500

3.7.2. pH impact on The IC dye degradation

The organic dye degradation takes place on the surface of nanomaterials, so the dye adsorption phenomena are an essential step in the photocatalytic rule. Earlier attempts stated that organic dye compounds with significant adsorption capability decompose quickly [50, 51]. Also, a greater pH value can provide a larger hydroxyl ions (OH^-) concentration to respond with holes and generate hydroxyl radicals ($^{\bullet}OH$), magnifying the dye photodegradation rate. Besides at below pH value, the before-mentioned IC dye will deliver a higher photodegradation appearance owing to the convenience of holes that will respond with water to create $^{\bullet}OH$. Therefore, the amount of adsorbed dye on the nanomaterial's surface and $^{\bullet}OH$ concentration will define the quantity of photodegradation [52]. The pH of the dye solution is a disturbing parameter in photodegradation experiments due to its influence on the ionization state, the surface phase catalyst, and the IC dye structure [53, 54]. Fig 9(a and b) represents the pH variation of IC dye photodegradation as a function of time and photocatalytic rate % in the pH range from 2 to 11.

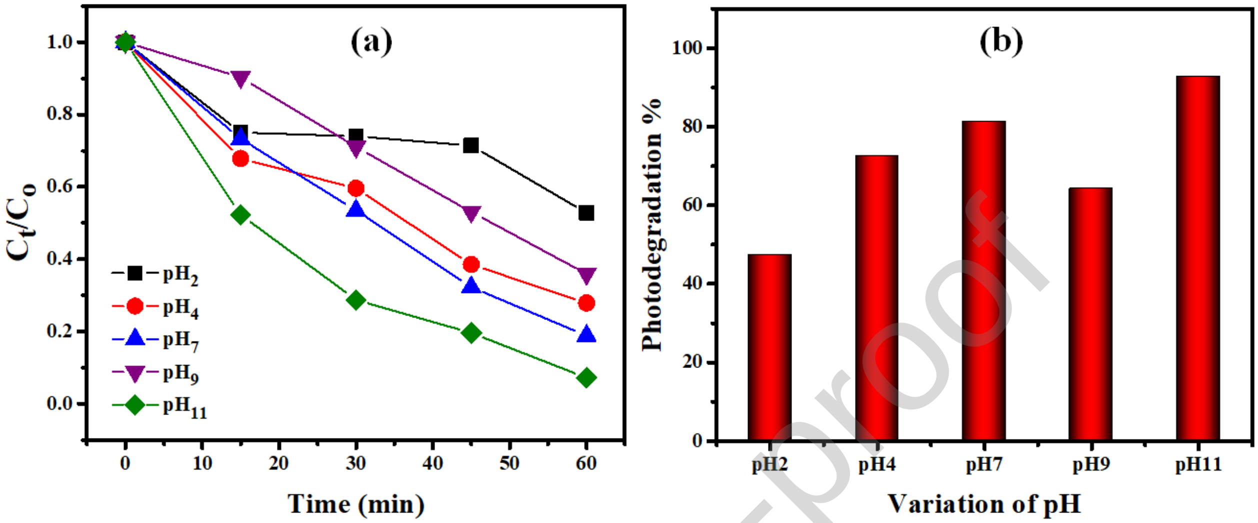

Fig 9: influence of pH variations on IC dye (a) photodegradation time and (b) photodegradation percentage

The results of photocomposite exhibit extremely weak capableness at pH in the acidic range. This behavior is because, at low pH, ZrO_2 present with ZrO_2@g-C_3N_4 nanostructures responds to the free H^+ in the water and is thoroughly destroyed in the solution. Besides, the H^+ complex with the negatively charged IC dye diminishes the electrostatic interactions force with active sites ZrO_2@g-C_3N_4 nanostructures [55]. Accordingly, the maximum pH necessary to destroy IC dye molecules is the neutral conditions when the best competence occurs (i.e., at pH 7).

3.7.3. Radical Scavengers Assessment

The radical trapping factors were examined to determine the effectiveness of radicals that contribute to dye degradation. Fig. 10 illustrates the IC dye photodegradation percentage rate *versus* t using a different scavenger. The results demonstrated that dye degradation yields are 82, 39, 90, 20, and 93%, which quenched with the interest of $AgNO_3$ (e^-) [54], EDTA (h^+) [56], IPA ($^\bullet OH$) [57], ASC ($^\bullet O_2^-$) [57], and free scavenger. The findings show a large reduction in the rate percentage IC dye photodegradation utilizing ASC, implying a vital purpose of $^{\bullet}O_2^-$ [58] in the degradation method.

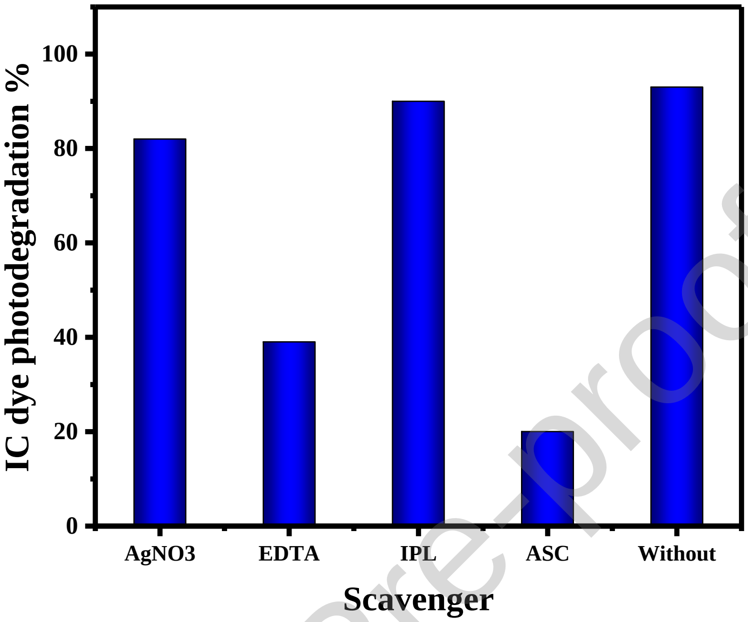

Fig 10: the reactive varieties trapping test of IC dye photodegradation via ZrO_2@g-C_3N_4 nanostructures

A significant position of holes (h^+) in the destruction activity is displayed by the strong influence of the EDTA on the IC dye photodegradation [59]. Alternatively, a second part is performed during the $^{\bullet}OH$ radicals [60] as designated by the weaker influence of its scavenger, the IPL, whereas there is no impact of nitric acid on the IC dye decolorization rule intimates no direct relationship electrons in the IC dye degradation [12]. This impact of scavenger results demonstrated that $^{\bullet}O_2^-$ and h^+ are playing principal reactive species in the IC dye catalytic degradation by ZrO_2@gC_3N_4 photocomposite.

3.7.4. The IC dye photodegradation Mechanism

Determined CB and VB values of ZrO_2@gC_3N_4 are obtained using the expressions [61]:

$$E_{CB} = X - E_C - 0.5\ E_g$$

$$E_{VB} = E_{CB} + E_g$$

where X corresponds to the semiconductor's absolute electronegativity (X for g-C_3N_4 and Zr O_2 are 4.72 and 5.91 respectively) [29, 62, 63], E_C corresponds to the free electron energy on the hydrogen scale (≈ 4.5 eV) and E_g is the band-gap energy of the semiconductor. The conduction and valence band potentials respectively presented as E_{CB} and VB. The CB and VB band-gap locations for g-C_3N_4 and ZrO_2 are therefore -1.170 and 1.700 eV, and -0.465 and 3.285 eV, respectively.

The boosted photodegradation performance of binal composite may be attributed to the simulated photocatalytic Z-scheme model playing a vital role in the photogenerated charge carriers' spatial separation [64]. Conferring to the scavengers' findings, it was proven that $^{\bullet}O_2^-$ and e^- primarily contributed to the photodegradation procedure. As visible light illumination strikes the g-C_3N_4 surface, it absorbs the light photons. Subsequently, the excited electrons acquire energy to get exalted from the VB to the CB, leaving behind the holes (h^+) [65]. Because of the direct contact among the composite semiconductors, the photo-excited electrons get conveyed from the g-C_3N_4 CB to the ZrO_2 CB; therefore, the 3D separation of electrons and holes occurs [66]. The electrons can then act the adsorbed oxygen on the composite surface and generate the reactive $^{\bullet}O_2^-$ ($O_2/^{\bullet}O_2^-$ = - 0.33 eV vs. NHE) [67]. However, the edges potential of VB for g-C_3N_4 (1.70 eV vs. NHE) is less favourable compared to the oxidation potential of $OH^-/^{\bullet}OH$ (2.40 V vs. NHE). Accordingly, the holes on the g-C_3N_4's VB cannot react with hydroxide ions to form the $^{\bullet}OH$ [49], as the radicals scavengers assessment proved. So, the photocatalytic dye elimination was accomplished by direct oxidation with the generated holes (h^+) on the g-C_3N_4 VB and the $^{\bullet}O_2^-$ inducted from photo-excited e^-s. This process is possibly improved by the affinity of H_2SO_4 anionic groups of the dye to the VB-holes, which motivates their sorption on the nanocomposite surface to perform the oxidation [68]. The significant difference between the migration rate of the photogenerated e^{-} and h^{+} may rationalize the $^{\bullet}O_2^{-}$ production. The following reaction with the dye molecules would be more expeditious than its direct oxidation by holes [28].

Consequently, this mechanism concurs adequately with the scavengers' processes imply that $^{\bullet}O_2^{-}$ and h^{+} are the effective species for the dye photodegradation utilizing the ZrO_2@g-C_3N_4 nanocomposite. This mechanism is in agreement with a similar study that investigated the generation of $^{\bullet}OH$ on the TiO_2/C_3N_4 surface through $C_6H_4(CO_2H)_2$ (TA) where no $^{\bullet}OH$ was identified. This phenomenon was attributed to the lower edges potential VB of g-C_3N_4 compared to that of $OH^{-}/^{\bullet}OH$ couple potentials [49]. Therefore, the proposed photodegradation Z-scheme mechanism's model advocates the formation of excess $^{\bullet}O_2^{-}$ along with additional powerful oxidizing agents' h^{+} than in the 'type II-heterojunction' one. This assumption is consistent with the experiments of scavenger to support the presumed Z-scheme mechanism path in the photodegradation of the tested dye [69]. Fig. 11 exemplifies the plausible mechanism of the dye molecule degradation process.

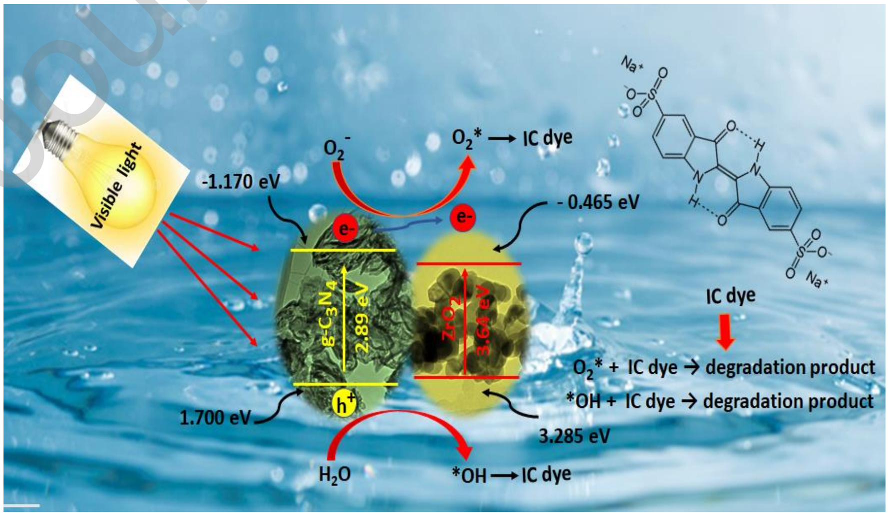

Fig 11: Scheme of IC dye photodegradation mechanism using ZrO_2@g-C_3N_4 nanocomposite

Table 2: A comparison of the ZrO_2@g-C_3N_4 photodegradation efficiency with other composites from literature.

Photocatalyst	**IC Photodegradation time**	***k* (min^{-1})**	**Ref.**
Cobalt doped ZrO_2	90 min	0.0024	[70]
ZnO/CuO/Si nanocomposite	85 min	0.0220	[71]
Mg doping ZnO nanoparticles	90 min	0.0087	[72]
TiO_2 quantum dots	120 min	0.0230	[73]
Mg/ZnO nanomaterials	90 min	0.0180	[72]
Multi-element doped ZrO_2	150 min	0.0100	[74]
(CuO + NiO)/AMSNC	60 min	0.0148	[75]
CaO nanomaterials	70 min	0.0149	[76]
alkali-activated magnesium	60 min	0.0124	[75]
ZrO_2@g-C_3N_4 photocomposite	**60 min**	**0.0279**	**This work**

A comparison of IC dye photocatalytic degradation with several nanomaterials' catalysts found in the literature is displayed in Table 2. The findings demonstrate the type of nanomaterials, rate of photodegradation, and IC Photodegradation time for various photocatalysts. The existing activity of ZrO_2@g-C_3N_4 photocomposite utilizes visible radiation for photodegradation of IC dye associated with additional activities related. The contemporary ZrO_2@g-C_3N_4 nanomaterial has the better photocatalytic ability for IC dye destruction.

3.7.5. Repeatability and reusability studies

The photocatalyst must be reusable and exhibit high repeatability to be effective in photocatalytic application. The photodegradation process was done three times under the same conditions to determine the repeatability of the IC dye degradation on the $ZrO_2@g\text{-}C_3N_4$ photocomposite. As illustrated in Fig. 12 a, the photodegradation rates of IC dyes stay nearly constant throughout the degradation processes, indicating high repeatability in photodegradation measurement. The reusability of the utilized photocatalyst is critical for meeting financial requirements. For this reason, the photodegradation and regeneration processes must be repeated to validate the photocatalyst application. The utilized $ZrO_2@g\text{-}C_3N_4$ photocomposite was regenerated by calcining for one hour at 776 K under the same optimized experimental conditions. The suspension was filtered after each experiment, and the photocatalyst was washed several times with distilled water, calcined at 776 K, and reused. Fig. 12 b illustrates the regeneration process. The photodegradation percentage of IC is found to be near 90% after three cycles, indicating that the $ZrO_2@g\text{-}C_3N_4$ photocomposite has the potential to be used efficiently for IC photodegradation.

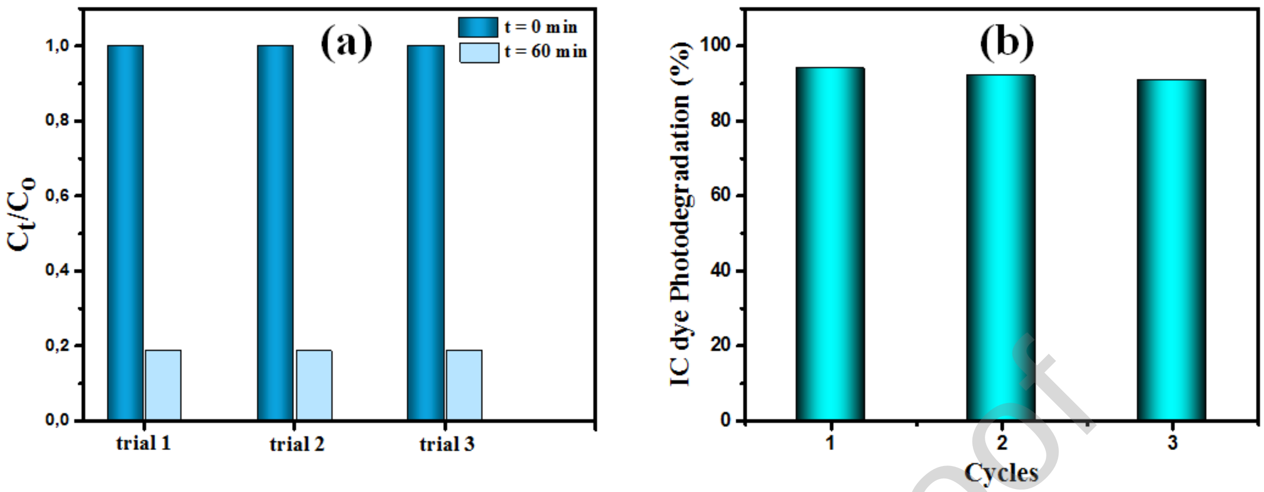

Figs. 12**:** Photocatalytic repeatability (a) irradiated and reusability (b) for IC degradation

4- Conclusion

$ZrO_2@g\text{-}C_3N_4$ photocatalyst was developed through ultrasonication in the existence of methanol solvent, and the obtained nanomaterials were annealed at 183 ^oC for 120 mins. The characterization of fabricated nanomaterials using various analytical devices proved the fabrication of $ZrO_2@g\text{-}C_3N_4$ nanocomposite with a higher surface area and lowering energy band-gap of 2.86 eV. Photocatalytic properties of ZrO_2 nanoparticles, $g\text{-}C_3N_4$ nanosheets, and $ZrO_2@g\text{-}C_3N_4$ nanocomposite were described via decomposed IC dye under visible irradiation. The $ZrO_2@g\text{-}C_3N_4$ nanocomposite provided great photodegradation production compared with the ZrO_2 and pure $g\text{-}C_3N_4$ nanosheets. The photodegradation experimental data were affirmed to obey the Lagergren kinetics model. Moreover, the $ZrO_2@g\text{-}C_3N_4$ photocomposite has a greater degradation rate constant (68 times) and lower half-life time values (0.25 times) than using pure $g\text{-}C_3N_4$. The impact of pH variation and the photocatalytic degradation mechanism of IC dye using $ZrO_2@g\text{-}C_3N_4$ nanocomposite were also investigated. The proposed photodegradation Z-scheme mechanism's model advocates the formation of excess $^{\bullet}O_2^-$ along with additional powerful oxidizing agents' h^+ than in the 'type II-heterojunction' one. From the obtained findings, it can be concluded that the ZrO2@g-C3N4 photocomposite, fabricated through a simplistic step ultra-sonication procedure, can be used as an effective catalyst to eliminate organic compounds from wastewater.

5-Acknowledgements

The authors extend their appreciation to the Deanship of Scientific Research at Imam Mohammad Ibn Saud Islamic University for funding this work through Research Group no. RG-21-09-70.

References:

[1] W. Ouyang, Y. Ji, S. Tan, Q. Tian, Z. Tong, Visible-light-response g-C3N4@ N, S-TiO2 nanocomposites for superior photocatalysis and photoelectrochemical performance, Journal of Alloys and Compounds, 866 (2021) 158964.

[2] Y. Ji, Y. Deng, F. Chen, Z. Wang, Y. Lin, Z. Guan, Ultrathin Co3O4 nanosheets anchored on multi-heteroatom doped porous carbon derived from biowaste for high performance solid-state supercapacitors, Carbon, 156 (2020) 359-369.

[3] W. Luo, X. Chen, Z. Wei, D. Liu, W. Yao, Y. Zhu, Three-dimensional network structure assembled by g-C3N4 nanorods for improving visible-light photocatalytic performance, Applied Catalysis B: Environmental, 255 (2019) 117761.

[4] Y. Chen, W. Lu, H. Shen, Y. Gu, T. Xu, Z. Zhu, G. Wang, W. Chen, Solar-driven efficient degradation of emerging contaminants by g-C3N4-shielding polyester fiber/TiO2 composites, Applied Catalysis B: Environmental, 258 (2019) 117960.

[5] M. Ismael, A review on graphitic carbon nitride (g-C3N4) based nanocomposites: synthesis, categories, and their application in photocatalysis, Journal of Alloys and Compounds, (2020) 156446.

[6] S. Yan, Z. Li, Z. Zou, Photodegradation performance of g-C3N4 fabricated by directly heating melamine, Langmuir, 25 (2009) 10397-10401.

[7] X. Hu, H. Ji, F. Chang, Y. Luo, Simultaneous photocatalytic Cr (VI) reduction and 2, 4, 6-TCP oxidation over g-C3N4 under visible light irradiation, Catalysis Today, 224 (2014) 34-40.

[8] C. Zhang, Z. Fu, F. Hong, G. Pang, T. Dong, Y. Zhang, G. Liu, X. Dong, J. Wang, Non-metal group doped g-C3N4 combining with BiF3: Yb3+, Er3+ upconversion nanoparticles for photocatalysis in UV–Vis–NIR region, Colloids and Surfaces A: Physicochemical and Engineering Aspects, 627 (2021) 127180.

[9] W. Liu, C. Song, M. Kou, Y. Wang, Y. Deng, T. Shimada, L. Ye, Fabrication of ultra-thin g-C3N4 nanoplates for efficient visible-light photocatalytic H2O2 production via two-electron oxygen reduction, Chemical Engineering Journal, (2021) 130615.

[10] Y. Li, X. Wang, X. Wang, Y. Xia, A. Zhang, J. Shi, L. Gao, H. Wei, W. Chen, Z-scheme BiVO4/g-C3N4 heterojunction: an efficient, stable and heterogeneous catalyst with highly enhanced photocatalytic activity towards Malachite Green assisted by H2O2 under visible light, Colloids and Surfaces A: Physicochemical and Engineering Aspects, 618 (2021) 126445.

[11] A. Toghan, A. Modwi, Boosting unprecedented indigo carmine dye photodegradation via mesoporous MgO@ g-C3N4 nanocomposite, Journal of Photochemistry and Photobiology A: Chemistry, 419 (2021) 113467.

[12] A. Toghan, H.M. Abd El-Lateef, K.K. Taha, A. Modwi, Mesoporous TiO2@ g-C3N4 composite: Construction, characterization, and boosting indigo carmine dye destruction, Diamond and Related Materials, (2021) 108491.

[13] J. Zhang, M. Zhang, R.Q. Sun, X. Wang, A facile band alignment of polymeric carbon nitride semiconductors to construct isotype heterojunctions, Angewandte Chemie International Edition, 51 (2012) 10145-10149.

[14] J. Hong, X. Xia, Y. Wang, R. Xu, Mesoporous carbon nitride with in situ sulfur doping for enhanced photocatalytic hydrogen evolution from water under visible light, Journal of Materials Chemistry, 22 (2012) 15006-15012.

[15] Y. Wang, Z. Wang, S. Muhammad, J. He, Graphite-like C 3 N 4 hybridized ZnWO 4 nanorods: Synthesis and its enhanced photocatalysis in visible light, CrystEngComm, 14 (2012) 5065-5070.

[16] K. Takanabe, K. Kamata, X. Wang, M. Antonietti, J. Kubota, K. Domen, Photocatalytic hydrogen evolution on dye-sensitized mesoporous carbon nitride photocatalyst with magnesium phthalocyanine, Physical Chemistry Chemical Physics, 12 (2010) 13020-13025.

[17] X. Wang, K. Maeda, A. Thomas, K. Takanabe, G. Xin, J.M. Carlsson, K. Domen, M. Antonietti, A metal-free polymeric photocatalyst for hydrogen production from water under visible light, Nature materials, 8 (2009) 76-80.

[18] G. Zhang, J. Zhang, M. Zhang, X. Wang, Polycondensation of thiourea into carbon nitride semiconductors as visible light photocatalysts, Journal of Materials Chemistry, 22 (2012) 8083-8091.

[19] Z. Zhao, Y. Sun, F. Dong, Graphitic carbon nitride based nanocomposites: a review, Nanoscale, 7 (2015) 15-37.

[20] T. Tang, L. You, P. Liang, T. Jia, W. Feng, Q. Liu, F. Li, W. Zhu, D. Wang, J. Wu, Tuning dimensionality TiO2/g-C3N4 heterostructure for enhanced elemental mercury removal performance under visible-light, Chemical Physics Letters, (2021) 139027.

[21] D. Neena, M. Humayun, D. Bhattacharyya, D. Fu, Hierarchical Sr-ZnO/g-C3N4 heterojunction with enhanced photocatalytic activities, Journal of Photochemistry and Photobiology A: Chemistry, 396 (2020) 112515.

[22] Y. Wang, X. Bai, C. Pan, J. He, Y. Zhu, Enhancement of photocatalytic activity of Bi 2 WO 6 hybridized with graphite-like C 3 N 4, Journal of Materials Chemistry, 22 (2012) 11568-11573.

[23] J. Fu, B. Chang, Y. Tian, F. Xi, X. Dong, Novel C 3 N 4–CdS composite photocatalysts with organic–inorganic heterojunctions: in situ synthesis, exceptional activity, high stability and photocatalytic mechanism, Journal of Materials Chemistry A, 1 (2013) 3083-3090.

[24] Y. Yu, W. Yan, X. Wang, P. Li, W. Gao, H. Zou, S. Wu, K. Ding, Surface engineering for extremely enhanced charge separation and photocatalytic hydrogen evolution on g-C3N4, Advanced materials, 30 (2018) 1705060.

[25] J.R. Xavier, Electrochemical and Mechanical Investigation of Newly Synthesized NiO-ZrO 2 Nanoparticle–Grafted Polyurethane Nanocomposite Coating on Mild Steel in Chloride Media, Journal of Materials Engineering and Performance, 30 (2021) 1554-1566.

[26] V.R. Channu, R.R. Kalluru, M. Schlesinger, M. Mehring, R. Holze, Synthesis and characterization of ZrO2 nanoparticles for optical and electrochemical applications, Colloids and Surfaces A: Physicochemical and Engineering Aspects, 386 (2011) 151-157.

[27] N. Gonçalves, J. Carvalho, Z. Lima, J. Sasaki, Size–strain study of NiO nanoparticles by X-ray powder diffraction line broadening, Materials Letters, 72 (2012) 36-38.

[28] Y. Li, J. Wang, Y. Yang, Y. Zhang, D. He, Q. An, G. Cao, Seed-induced growing various TiO2 nanostructures on g-C3N4 nanosheets with much enhanced photocatalytic activity under visible light, Journal of hazardous materials, 292 (2015) 79-89.

[29] X. Bi, S. Yu, E. Liu, X. Yin, Y. Zhao, W. Xiong, Nano-zirconia supported by graphitic carbon nitride for enhanced visible light photocatalytic activity, RSC Advances, 10 (2020) 524-532.

[30] C. Feng, Y. Deng, L. Tang, G. Zeng, J. Wang, J. Yu, Y. Liu, B. Peng, H. Feng, J. Wang, Applied Catalysis B: environmental performance for enhanced full-spectrum-light photocatalytic activities, Appl. Catal. B Environ., 239 (2018) 525-536.

[31] X. Wang, L. Zhang, H. Lin, Q. Nong, Y. Wu, T. Wu, Y. He, Synthesis and characterization of a ZrO 2/gC 3 N 4 composite with enhanced visible-light photoactivity for rhodamine degradation, Rsc Advances, 4 (2014) 40029-40035.

[32] T. Muhmood, M. Xia, W. Lei, F. Wang, M.A. Khan, Efficient and stable ZrO 2/Fe modified hollow-C 3 N 4 for photodegradation of the herbicide MTSM, Rsc Advances, 7 (2017) 3966-3974.

[33] P. Niu, L. Zhang, G. Liu, H.M. Cheng, Graphene-like carbon nitride nanosheets for improved photocatalytic activities, Advanced Functional Materials, 22 (2012) 4763-4770.

[34] X.-H. Li, X. Wang, M. Antonietti, Solvent-free and metal-free oxidation of toluene using O2 and g-C3N4 with nanopores: nanostructure boosts the catalytic selectivity, Acs Catalysis, 2 (2012) 2082-2086.

[35] Z. Zhu, Z. Lu, X. Zhao, Y. Yan, W. Shi, D. Wang, L. Yang, X. Lin, Z. Hua, Y. Liu, Surface imprinting of a gC 3 N 4 photocatalyst for enhanced photocatalytic activity and selectivity towards photodegradation of 2-mercaptobenzothiazole, RSC Advances, 5 (2015) 40726-40736.

[36] A. Singh, U.T. Nakate, Microwave synthesis, characterization, and photoluminescence properties of nanocrystalline zirconia, The Scientific World Journal, 2014 (2014).

[37] M. Rezaei, M. Khajenoori, B. Nematollahi, Synthesis of high surface area nanocrystalline MgO by pluronic P123 triblock copolymer surfactant, Powder Technology, 205 (2011) 112-116.

[38] G.K. Sidhu, A.K. Kaushik, S. Rana, S. Bhansali, R. Kumar, Photoluminescence quenching of Zirconia nanoparticle by surface modification, Applied Surface Science, 334 (2015) 216-221.

[39] N. Mao, J.-X. Jiang, MgO/g-C3N4 nanocomposites as efficient water splitting photocatalysts under visible light irradiation, Applied Surface Science, 476 (2019) 144-150.

[40] L. Ge, C. Han, Synthesis of MWNTs/g-C3N4 composite photocatalysts with efficient visible light photocatalytic hydrogen evolution activity, Applied Catalysis B: Environmental, 117 (2012) 268-274.

[41] H. Ji, F. Chang, X. Hu, W. Qin, J. Shen, Photocatalytic degradation of 2, 4, 6-trichlorophenol over g-C3N4 under visible light irradiation, Chemical Engineering Journal, 218 (2013) 183-190.

[42] S. Velu, K. Suzuki, C.S. Gopinath, H. Yoshida, T. Hattori, XPS, XANES and EXAFS investigations of CuO/ZnO/Al 2 O 3/ZrO 2 mixed oxide catalysts, Physical Chemistry Chemical Physics, 4 (2002) 1990-1999.

[43] P. Ragupathy, D.H. Park, G. Campet, H. Vasan, S.-J. Hwang, J.-H. Choy, N. Munichandraiah, Remarkable capacity retention of nanostructured manganese oxide upon cycling as an electrode material for supercapacitor, The Journal of Physical Chemistry C, 113 (2009) 6303-6309.

[44] M. Ismael, Y. Wu, M. Wark, Photocatalytic activity of ZrO 2 composites with graphitic carbon nitride for hydrogen production under visible light, New Journal of Chemistry, 43 (2019) 4455-4462.

[45] P. Chen, P. Xing, Z. Chen, X. Hu, H. Lin, L. Zhao, Y. He, In-situ synthesis of AgNbO3/g-C3N4 photocatalyst via microwave heating method for efficiently photocatalytic H2 generation, Journal of colloid and interface science, 534 (2019) 163-171.

[46] Z. Chen, P. Chen, P. Xing, X. Hu, H. Lin, L. Zhao, Y. Wu, Y. He, Rapid fabrication of KTa0. 75Nb0. 25/g-C3N4 composite via microwave heating for efficient photocatalytic H2 evolution, Fuel, 241 (2019) 1-11.

[47] X. Wang, S. Wang, W. Hu, J. Cai, L. Zhang, L. Dong, L. Zhao, Y. He, Synthesis and photocatalytic activity of SiO2/g-C3N4 composite photocatalyst, Materials Letters, 115 (2014) 53-56.

[48] A. Modwi, M. Abbo, E. Hassan, A. Houas, Effect of annealing on physicochemical and photocatalytic activity of Cu5% loading on ZnO synthesized by sol–gel method, Journal of Materials Science: Materials in Electronics, 27 (2016) 12974-12984.

[49] J. Yu, S. Wang, J. Low, W. Xiao, Enhanced photocatalytic performance of direct Z-scheme gC 3 N 4–TiO 2 photocatalysts for the decomposition of formaldehyde in air, Physical Chemistry Chemical Physics, 15 (2013) 16883-16890.

[50] C.A. Gouvea, F. Wypych, S.G. Moraes, N. Duran, N. Nagata, P. Peralta-Zamora, Semiconductor-assisted photocatalytic degradation of reactive dyes in aqueous solution, Chemosphere, 40 (2000) 433-440.

[51] M. Anas, D.S. Han, K. Mahmoud, H. Park, A. Abdel-Wahab, Photocatalytic degradation of organic dye using titanium dioxide modified with metal and non-metal deposition, Materials Science in Semiconductor Processing, 41 (2016) 209-218.

[52] J.M. Gutteridge, D.A. Rowley, B. Halliwell, Superoxide-dependent formation of hydroxyl radicals in the presence of iron salts. Detection of 'free'iron in biological systems by using bleomycin-dependent degradation of DNA, Biochemical Journal, 199 (1981) 263-265.

[53] E. Fathi, F. Derakhshanfard, P. Gharbani, Z.G. Tabatabaei, Facile Synthesis of MgO/C3N4 Nanocomposite for Removal of Reactive Orange 16 Under Visible Light, Journal of Inorganic and Organometallic Polymers and Materials, 30 (2020) 2234-2240.

[54] A. Modwi, M.B. Aissa, K.K. Taha, L. Khezami, J. El Ghoul, A.S. Al-Ayed, M. Bououdina, Fabrication of (Y 2 O 3) n–ZnO nanocomposites by high-energy milling as potential photocatalysts, Journal of Materials Science: Materials in Electronics, 32 (2021) 3415-3430.

[55] L.G. Devi, S.G. Kumar, Influence of physicochemical–electronic properties of transition metal ion doped polycrystalline titania on the photocatalytic degradation of Indigo Carmine and 4-nitrophenol under UV/solar light, Applied Surface Science, 257 (2011) 2779-2790.

[56] H. Zhang, R. Zong, Y. Zhu, Photocorrosion inhibition and photoactivity enhancement for zinc oxide via hybridization with monolayer polyaniline, The Journal of Physical Chemistry C, 113 (2009) 4605-4611.

[57] J. Lv, K. Dai, J. Zhang, Q. Liu, C. Liang, G. Zhu, Facile constructing novel 2D porous g-C3N4/BiOBr hybrid with enhanced visible-light-driven photocatalytic activity, Separation and Purification Technology, 178 (2017) 6-17.

[58] Q. Zhang, J. Bai, G. Li, C. Li, Synthesis and enhanced photocatalytic activity of AgI-BiOI/CNFs for tetracycline hydrochloride degradation under visible light irradiation, Journal of solid state chemistry, 270 (2019) 129-134.

[59] H. Tang, S. Chang, L. Jiang, G. Tang, W. Liang, Novel spindle-shaped nanoporous TiO2 coupled graphitic g-C3N4 nanosheets with enhanced visible-light photocatalytic activity, Ceramics International, 42 (2016) 18443-18452.

[60] Z. Tong, D. Yang, T. Xiao, Y. Tian, Z. Jiang, Biomimetic fabrication of g-C3N4/TiO2 nanosheets with enhanced photocatalytic activity toward organic pollutant degradation, Chemical Engineering Journal, 260 (2015) 117-125.

[61] R. Senthil, J. Theerthagiri, A. Selvi, J. Madhavan, Synthesis and characterization of low-cost g-C3N4/TiO2 composite with enhanced photocatalytic performance under visible-light irradiation, Optical Materials, 64 (2017) 533-539.

[62] A. Albouyeh, A. Pourahmad, H. Kefayati, The green synthesis of magnesium oxide nanoparticles in MFI type zeolite and its application as a photocatalyst, Journal of Water and Environmental Nanotechnology, 5 (2020) 283-293.

[63] S. Martha, K.H. Reddy, K. Parida, Fabrication of In_2O_3 modified ZnO for enhancing stability, optical behaviour, electronic properties and photocatalytic activity for hydrogen production under visible light, (2014).

[64] T. Ohno, N. Murakami, T. Koyanagi, Y. Yang, Photocatalytic reduction of CO2 over a hybrid photocatalyst composed of WO3 and graphitic carbon nitride (g-C3N4) under visible light, Journal of CO2 Utilization, 6 (2014) 17-25.

[65] R. Aaberge, Ø. Kravdal, T. Wennemo, Unobserved heterogeneity in models of marriage dissolution, Discussion Papers, 1989.

[66] L.G. Devi, R. Kavitha, A review on plasmonic metal☐ TiO2 composite for generation, trapping, storing and dynamic vectorial transfer of photogenerated electrons across the Schottky junction in a photocatalytic system, Applied Surface Science, 360 (2016) 601-622.

[67] H. Li, S. Gan, H. Wang, D. Han, L. Niu, Intercorrelated superhybrid of AgBr supported on graphitic-C3N4-decorated nitrogen-doped graphene: high engineering photocatalytic activities for water purification and CO2 reduction, Advanced materials, 27 (2015) 6906-6913.

[68] R.E. Palma-Goyes, J. Silva-Agredo, I. González, R.A. Torres-Palma, Comparative degradation of indigo carmine by electrochemical oxidation and advanced oxidation processes, Electrochimica acta, 140 (2014) 427-433.

[69] N. Omrani, A. Nezamzadeh-Ejhieh, A ternary Cu2O/BiVO4/WO3 nano-composite: Scavenging agents and the mechanism pathways in the photodegradation of sulfasalazine, Journal of Molecular Liquids, 315 (2020) 113701.

[70] W.W. Anku, S.O.-B. Oppong, S.K. Shukla, E.S. Agorku, P.P. Govender, Cobalt doped ZrO2 decorated multiwalled carbon nanotube: a promising nanocatalyst for photodegradation of indigo carmine and eosin Y dyes, Progress in Natural Science: Materials International, 26 (2016) 354-361.

[71] A. Dhara, A. Baral, S. Chabri, A. Sinha, N.R. Bandyopadhyay, N. Mukherjee, An efficient approach towards the photodegradation of indigo carmine by introducing ZnO/CuO/Si ternary nanocomposite as photocatalyst, Journal of The Institution of Engineers (India): Series D, 98 (2017) 1-8.

[72] P. Labhane, S. Sonawane, G. Sonawane, S. Patil, V. Huse, Influence of Mg doping on ZnO nanoparticles decorated on graphene oxide (GO) crumpled paper like sheet and its high photo

catalytic performance under sunlight, Journal of Physics and Chemistry of Solids, 114 (2018) 71-82.

[73] S. Sood, S. Kumar, A. Umar, A. Kaur, S.K. Mehta, S.K. Kansal, TiO2 quantum dots for the photocatalytic degradation of indigo carmine dye, Journal of Alloys and Compounds, 650 (2015) 193-198.

[74] E. Agorku, A. Kuvarega, B. Mamba, A. Pandey, A. Mishra, Enhanced visible-light photocatalytic activity of multi-elements-doped ZrO2 for degradation of indigo carmine, Journal of rare earths, 33 (2015) 498-506.

[75] Y.J. Zhang, L. Kang, L.C. Liu, H.X. Si, J.F. Zhang, Synthesis of a novel alkali-activated magnesium slag-based nanostructural composite and its photocatalytic performance, Applied Surface Science, 331 (2015) 399-406.

[76] K. Devarahosahalli Veeranna, M. Theeta Lakshamaiah, R. Thimmasandra Narayan, Photocatalytic degradation of indigo carmine dye using calcium oxide, International Journal of Photochemistry, 2014 (2014).

Author contribution statement

L. Khezami: Conceptualization, writing original draft preparation, supervision; M. Ali Ben Aissa: writing, review , A Modwi: writing, review, Mokhtar Ismail: writing, review, Ahlem Guesmi: writing, review, F. K. Algethami¨: writing, review, Manel Ben Ticha: writing, review, Aymen Amine Assadi˸ writing, validation, review the final version, P. Nguyen-Tri: writing, validation, supervision, review the final version

Conflict of interest statement

The authors declare that they have no known competing financial interests or personal relationships that could have appeared to influence the work reported in this paper

Highlights

- ZrO_2@g-C_3N_4 nanocomposite was ultrasonically fabricated using the precursors ZrO_2 and g-C_3N_4.
- The anchoring of ZrO_2 and g-C_3N_4 was verified by XPS, XRD, and EDX techniques.
- The nanocomposite has proficiently degraded the indigo carmine dye during a visible-light-driven process.
- A Z-scheme model was suggested for the enhancement as confirmed through the $^{\bullet}O_2^{-}$ and h^+ involvement.